ABSTRACT

BALLANCE, BRANDON WAYNE. Snapshot Imaging Laser Displacement Sensor for Hypersonic Diagnostic Testing. (Under the direction of Dr. Michael Kudenov).

Three Dimensional Digital Image Correlation (3D DIC) is a technique where two cameras are used to gather displacement information of an object in the X/Y/Z plane using the stereo vision method. Phase Modulated Interferometry (PMI) is a method that utilizes the change in phase of diffraction patterns projected onto an object to measure displacement. In this thesis, these two methods are combined to create a snapshot imaging laser displacement sensor that will be able to measure displacement of an object in hypersonic environments (such as a hypersonic wind tunnel). Inside a hypersonic environment, the index medium is constantly changing due to turbulence. As this medium changes, the chief ray path from the object to the camera is altered, therefore disallowing proper measurement of the object's deformation using 3D DIC. The inclusion of a diffraction pattern projected into this environment allows more degrees of freedom to account for this ray change. As the diffraction pattern is projected, it becomes altered as it reaches the target. This diffraction pattern changes due to object displacement and distortion of the mediums index of refraction. Using this diffraction pattern and an algorithm derived for this sensor, turbulence can be factored out of the system.

Final benchtop testing results are shown for the new system, and compared to 3D DIC using mean absolute error between the system's measurement and a known measurement of the object. Current mean absolute error results are as low as 7 μm. This method is best used when measuring an object's displacement in an environment where contact measurement methods are not feasible. A discussion of the findings and future work conclude the thesis.

Snapshot Imaging Laser Displacement Sensor for Hypersonic Diagnostic Testing

by
Brandon Wayne Ballance

A thesis submitted to the Graduate Faculty of
North Carolina State University
in partial fulfillment of the
requirements for the degree of
Master of Science

Electrical Engineering

Raleigh, North Carolina
2019

APPROVED BY:

_____	_____
Dr. Michael Escuti	Dr. Tianfu Wu

_____
Dr. Michael Kudenov
Chair of Advisory Committee

DEDICATION

I would like to dedicate this to my family who have helped me through all my obstacles in life. Through their support I have taken on challenges I would never have dreamed of. I also want to dedicate this to my fiancé, who has supported me through many tough decisions and mixed feelings. Through her, I have been able to solidify my path in my professional career.

BIOGRAPHY

Brandon Ballance was born on March 22nd, 1994 in San Diego, California. Early in his life he moved more permanently to Holly Springs, North Carolina to complete the majority of his grade school. Brandon then went on to complete his undergraduate at North Carolina State University with a Bachelor of Science in Electrical Engineering in May of 2017. While in his undergraduate career, Brandon interned at many different companies including Tesla, Cree, and Siemens. He went on to stay at North Carolina State University for his Masters of Science in Electrical Engineering, joining the Optical Sensing Lab in August of 2017 as a Graduate Research Student. After earning his Master's degree, he plans to begin his professional career as a Senior Software Engineer at Lockheed Martin working on algorithm development.

ACKNOWLEDGMENTS

I would like to acknowledge my committee members: Dr. Michael Kudenov, Dr. Michael Escuti, and Dr. Tianfu Wu. They have all been able to guide me throughout my graduate student career, and have served as both great committee members and amazing professors. I would especially like to acknowledge Dr. Kudenov for the countless hours he has spent with me in his office, asking questions about code, interviewing, and many other miscellaneous subjects. Through him, I have been able to improve as an engineer in ways I had not ever considered. Because of him I have become a more focused and driven individual, and hope for the opportunity to apply everything I have learned later in my professional career.

I would also like to acknowledge the other research students in the Optical Sensing Lab and the Geometric Phase Lab. Through shared experience and group knowledge, we have all been able to help push each other through problems and become better teammates and friends. Without such an amazing group, getting through graduate school would have been a more daunting task.

Lastly, I would like to acknowledge Arnold Engineering Development Complex (AEDC) and Control Vision, Inc. (CVI) for backing this project and making all of my research possible.

TABLE OF CONTENTS

LIST OF TABLES

LIST OF FIGURES

1.0. Introduction

1.1. Project Goals

Driven by the desire to improve upon conventional digital image correlation methods within hypervelocity environments (such as hypersonic wind tunnels), the goal of this project is to develop a snapshot imaging laser displacement sensor capable of 3D profilometry with a measurement region 150 mm in diameter, a deflection depth measurement accurate to ±30 μm, a range of detectable motion of at least 60 mm, sampling rates exceeding 1 kHz (with profiles available in real time at 30 Hz), and a sensor resolution of 1600 x 1200 pixels.

1.2. Digital Image Correlation: Overview

Two-Dimensional digital image correlation (2D DIC) is an optical metrology based on digital image processing and numerical computing, and is a widely accepted form for in-plane deformation measurements of a planar object surface [1]. Due to its non-contact, non-destructive nature, DIC is important for measuring objects that are difficult to reach. 2D DIC is limited to in-plane measurements, due to only using a single camera in the system. If the object becomes more complex, such as having a curved surface or a three-dimensional (3D) deformation, 3D DIC is required. 3D DIC utilizes the principle of binocular stereovision. Since this project deals with cases of 3D deformations, it becomes more important to understand 3D DIC and stereovision. 3D DIC utilizes two cameras to obtain the 3D coordinates of a single point on the object. Figure 1 shows a diagram of this process. Point P is denoted as a single point whose location is being calculated. Points P_1 and P_2 represent the translation of point P on the camera plane. O_{c1} and O_{c2} represent the optical centers of each camera. It should be noted from Figure 1 that 2D DIC would not be possible due to its inability to measure depth. This has to do with the lack of being able to obtain points P_1 and P_2.

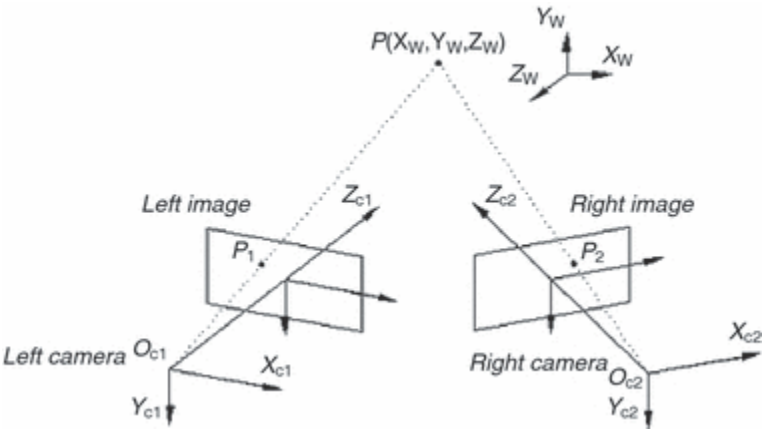

Figure 1: Schematic Diagram of 3D DIC Setup [2]

3D DIC has already been adopted in many applications, particularly in solid mechanics (due to its ability to measure deformation from applied mechanical or thermal loads), and is continually garnering interest in other engineering fields as well. In the case of this paper, a mechanical strain is being induced on the object tested by hypervelocity wind turbulence. Since the object in question cannot be accessed directly for utilizing a strain gauge measurement, 3D DIC is the best choice to make sure any 3D deformations are captured.

1.3. Interferometry: Overview

Interferometry is the use of light (as a wave) to create an interference pattern and utilize the interference pattern to extract information. There are many different interferometric techniques such as a wave front division and amplitude division. Among those techniques, different information can be extracted such as displacement, optical substrate quality, and index of refraction changes.

A good example that illustrates the concept of interferometry is Young's double slit experiment as depicted in Figure 2. This involves utilizing a point light source to emit a spherical wave that illuminates two slits [3]. The light is diffracted at each slit, creating two separate spherical waves that eventually create constructive or destructive interference onto a screen at

different points [3]. These interference patterns are known as fringes, which are the underlying phenomena (principles) behind all interferometric techniques.

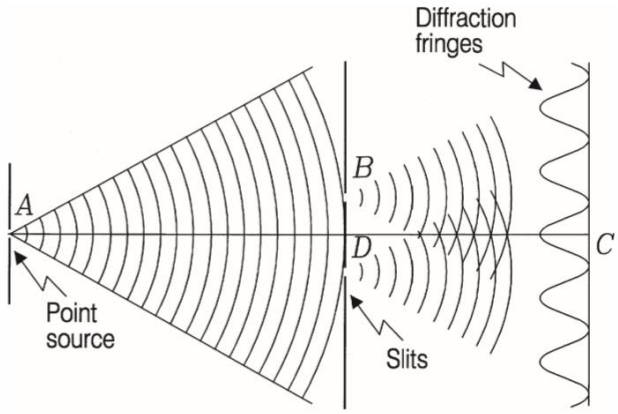

Figure 2: Basic Young's double slit experiment setup for observing interference fringes [3].

The work in this thesis relies on a particular approach of interferometry, known as phase measurement interferometry (PMI). A detailed discussion on that method is provided in section 2.2. In this section, an overview on PMI will be discussed.

For all techniques involving PMI, a temporal phase modulation is introduced in order to take a measurement [4]. Depending on the technique being used, the modulation will be introduced differently. Different ways for modulating the phase include moving a mirror, moving a grating, and using an electro-optic modulator (among many more) [4]. There are two ways to determine the phase: electronically and analytically [4]. Electronic requires the use of hardware such as zero-crossing detectors, phase-locked loops, and up-down counters while for analytical, intensity data is recorded temporally and is sent to a computer to calculate phase difference [4].

One example of an interferometric technique that utilizes PMI is synthetic aperture radar (SAR) interferometry. This technique utilizes phase information from complex radar data to extract three-dimensional information on the Earth's surface [5].

1.4. Overview of Thesis

This thesis focuses on utilizing a combination of digital image correlation and interferometry to obtain data that cannot be taken without the use of non-destructive techniques. An emphasis is then put on the algorithms used and developed specifically for this project to obtain accurate spatial measurements in relation to known benchtop measurements. Chapter two covers the optical system and how the decisions were made for the geometry of the system. Chapter three provides information behind the algorithms developed and used in this project. Chapter four describes the benchtop testing, the data collection at each algorithm, comparing the collected results with a known value. Chapter five concludes this thesis by evaluating the successfulness of this method and provides future work.

2.0. Optical System

The optical system used for this project utilizes different types of geometry, which are designed to account for turbulent flow. This chapter presents three topics based around the optical system, namely the reasoning behind the specific geometry of the system, the utilization of Wollaston Prisms to create a diffraction pattern, and an overview of the equipment used (such as the camera models, lens focal lengths, etc.) and tests performed.

2.1. Optical System Geometry

The optical system geometry is an important part of this project, as it allows for the use of the fringe projection optics to factor out turbulent effects on the DIC camera system. The system overview is depicted in Figure 3. An important parameter of this system is the separation between fringe optics and cameras.

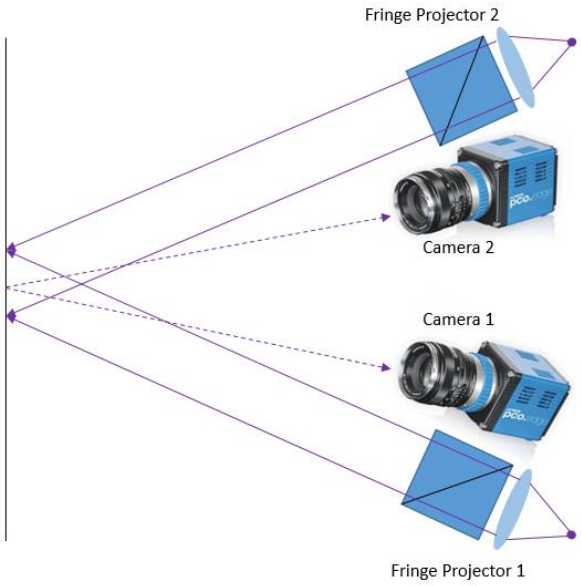

Figure 3: Layout overview of optical system

A careful design choice of the separation of fringe optics and camera will ensure that the fringe projection chief ray differentiates in optical path from the camera chief ray as the index of refraction within the tunnel environment is changing. Figure 4 depicts one side of the system in

relation to the turbulent flow, with geometric variables for the following derivation. These variables are described further below. This derivation is done as if the object is not moving, and displacement only occurs due to turbulence.

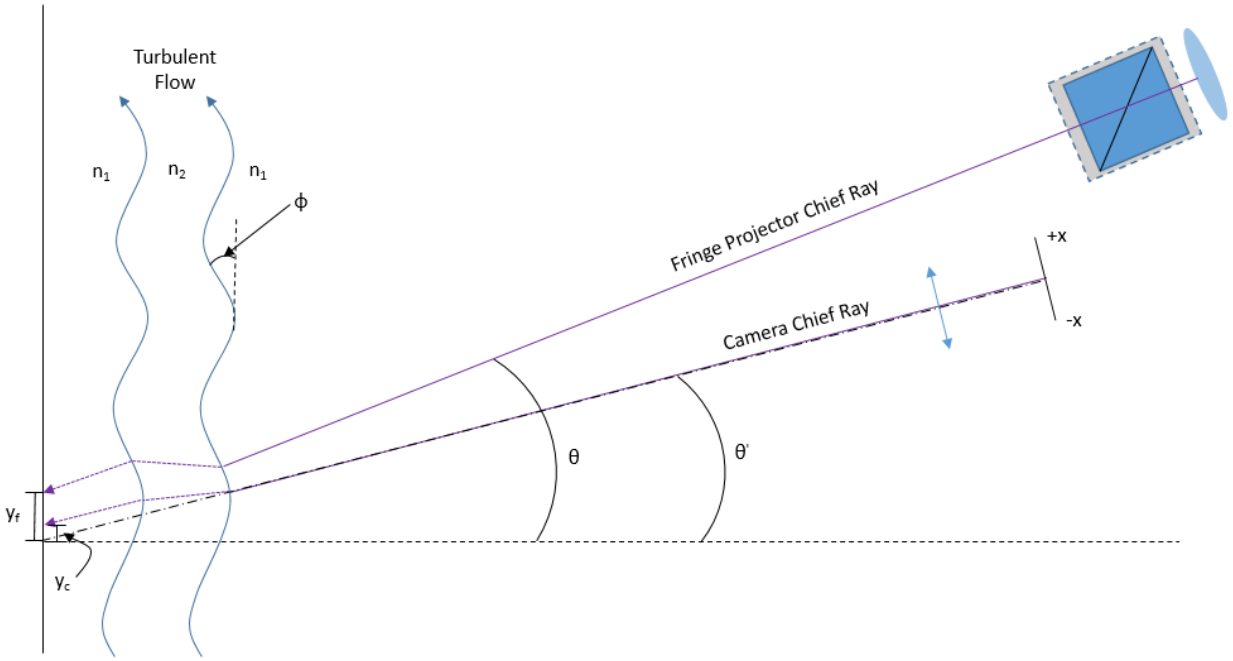

Figure 4: Close up of a single side of the optical system, including geometric variables and turbulence in the image. The line from the camera to the target is the chief ray as if it would have traveled to the target point of the fringe projector chief ray, but instead is being altered by turbulence

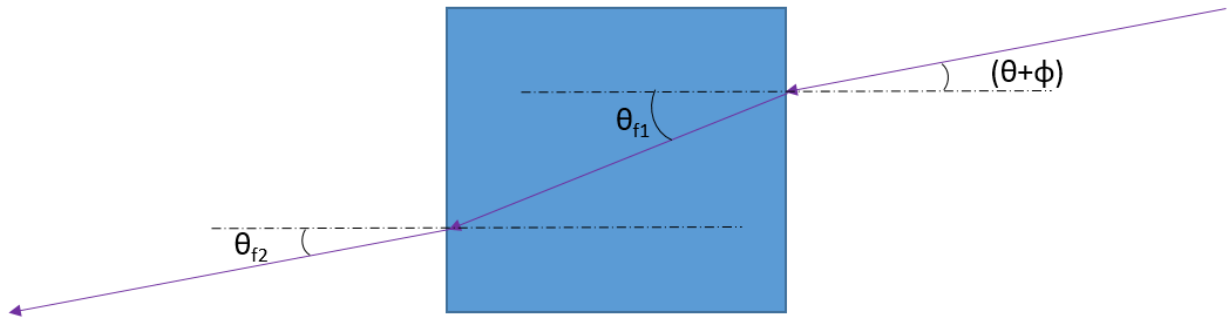

Figure 5: Close up of angles as they enter and leave turbulence medium. This represents a more simplistic view, and not that of actual turbulence

In Figure 4, θ is related to the separation of the fringe projector and normal of the target, φ relates to the tilt angle subject to a change in the medium index, and θ' relates to the angle of

the camera optical center and the normal of the target. $\theta_{f1,}$ $\theta_{f2,}$ θ_{c1} and θ_{c2} are shown in Figure 5. These angles refer to the angle between the ray of either the fringe projector (*f*) or camera (*c*) as it travels through a change in medium and the normal. This figure only depicts the fringe path. The camera path is similar, however the input angle becomes $(\theta'+\varphi)$ instead. $\theta_{f1,}$ $\theta_{f2,}$ θ_{c1} and θ_{c2} can be represented by equations (1), (2), (3) and (4) utilizing the small angle approximation of Snells Law.

$$\theta_{f1} = \frac{n1}{n2}(\theta+\varphi), \tag{1}$$

$$\theta_{f2} = \frac{n2}{n1}\theta_{f1} = (\theta+\varphi), \tag{2}$$

$$\theta_{c1} = \frac{n1}{n2}(\theta'+\varphi), \tag{3}$$

$$\theta_{c2} = \frac{n2}{n1}\theta_{c1} = (\theta'+\varphi). \tag{4}$$

Displacements y_f and y_c (displacement of the chief ray from the fringe projector to the object, and displacement of the chief ray from the camera to the object) can be represented by equations (5) and (6),

$$y_c = t*\tan(\theta_{f1}), \tag{5}$$

$$y_f = t*\tan(\theta_{c1}), \tag{6}$$

where *t* is the thickness of the medium with an index of refraction greater than air. It is desirable to make the angle between the camera and fringe projector as paraxial as possible, therefor equations (5) and (6) can be represented in the form of equation (7).

$$y = t*\theta \tag{7}$$

Equating equation (5) and (6) using thickness yields the following equation (8):

$$\frac{y_f}{\theta'+\varphi}=\frac{y_c}{\theta+\varphi}. \tag{8}$$

As the angle between the fringe projector and the camera approaches 0, θ’ becomes equal to θ. Referencing equation (8), as these two angles become equal, y_f becomes equal to y_c. If these two displacements are equal to each other, then the system will not be able to discern displacement caused by turbulence or displacement caused by target movement. This is due to the chief ray of the projector following the same path as the chief ray of the camera.

2.2. Fringe Projection Using Wollaston Prisms

Wollaston Prisms are polarizing beam splitting prisms, consisting of two prisms with a wedge angle α cemented on the hypotenuse [6]. When an unpolarized beam enters the first pism, the ordinary ray is retarded with respect to the extraordinary ray [6]. Once in the second prism, the two rays swap (ordinary ray becomes extraordinary, and vice versa) and the ordinary ray is now slower. This causes the ordinary ray to refract towards the interface’s normal while the extraordinary ray is refracted away. Figure 6 shows this setup with two right angle Wollaston Prisms.

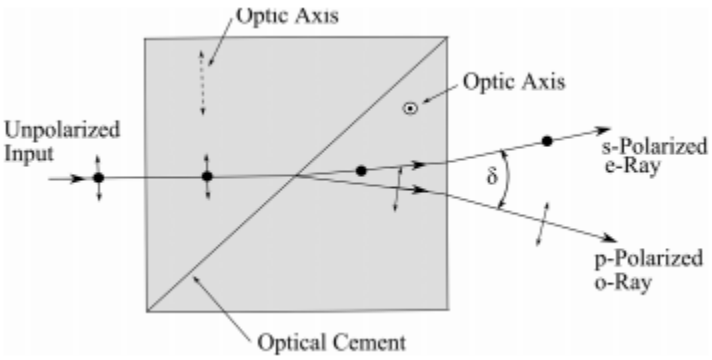

Figure 6: Right angle Wollaston Prisms [6]

The two Wollaston Prisms being used for fringe projection are made of quartz crystal and designed for a wavelength of 450 nm. The prism specifications include a wedge angle α of 5.45°, and a birefringence Δn of 0.0094. The diffraction pattern’s period on the object is

$$\Lambda = \frac{\lambda}{\Delta n \tan(\alpha)}. \quad (9)$$

The projected spatial period, calculated for the projector's Wollaston Prisms, is 501 μm.

2.3. Experimental Setup and Testing

The system utilizes a custom electronics board designed by the sponsor to control both the laser diodes and the cameras. This allows the master side to trigger the slave side. The imaging system uses Basler ACA1300-30GM cameras, with a fixed 50 mm focal length Nikon Lens set at f/11. A Thorlabs L450P1600MM laser diode is used. The light from the laser diode in the TCLDM9 TE-cooled Thorlabs mount is collimated using a 150 mm focal length lens. The collimated light then enters the Wollaston Prisms. Lastly the light passes through a linear polarizer with fast axis at zero degrees and projects onto the object. A basic overview of the laser optical system is shown in Figure 7. The object being imaged is a metal plate painted completely white, with a randomized black pattern painted on top for the optical flow algorithm. A randomized pattern is used so the algorithm used to measure displacement has something to track without any phase ambiguity. The plate is mounted on a Thorlabs linear translation stage. A piezoelectric actuator is mounted on the back of the stage to provide a known displacement to the object while being imaged, and is being driven by a signal generator. The angles used for the system geometry are shown in Table 1. The center line used is from the object.

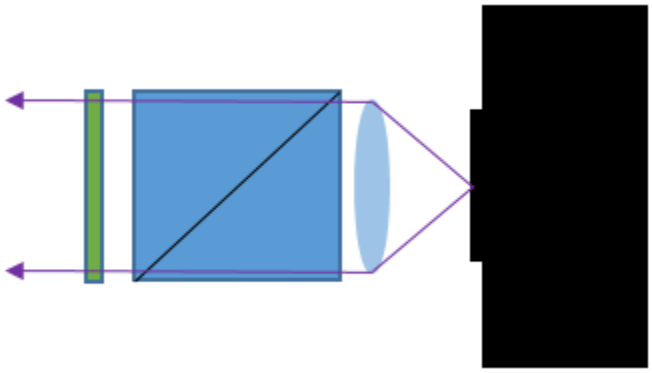

Figure 7: Optical System Overview

Table 1: Geometry for experimental setup

	Master	Slave
Fringe-Normal Angle	22.5°	-22.5°
Camera-Normal Angle	18°	-18°

Nine tests are performed. Each test is described in Table 2. For the test notes, either only fringes, only random dots (R.D), or a combination of both is used. Everything after test 3 is a combination of both. The first 3 tests are used to test each individual system/algorithm. When denoting “Only Fringes”, the fringes are projected onto a blank white object. When denoting “Only R.D”, the Wollaston Prisms are removed and a collimated beam is projected onto the object with the R.D pattern on it. Object displacement describes whether or not the object is being displaced with the piezoelectric actuator, as well as if it is being displaced enough to cause 2π ambiguity in the fringes. A test will either have no turbulence, static turbulence, or soft turbulence. Static turbulence is simulated using a 100 μm thick microscope cover glass. The glass is passed through the beam as close to the object as possible. Soft turbulence is simulated using a nichrome wire and a heat gun. The wire has current passed through it and as it heats up, “turbulence” is created in front of the object. The wire is set below the object so the heat travels through the beams. The heat gun turned on and pushes heat across the object, from side to side.

Table 2: Experimental Tests

Tests	Notes	Object Displacement	Turbulence
1	Static Object	Static	None
2	Only Fringes	$\Delta z<2\pi$	None
3	Only R.D.	$\Delta z<2\pi$	None
4	Fringes + R.D.	$\Delta z<2\pi$	None
5	2π Ambiguity, Fringes + R.D.	$\Delta z>2\pi$	None
6	Fixed Plate w/ Turb	Static	Static
7	Fixed Plate w/ Turb	Static	Soft
8	Moving Plate w/ Turb	$\Delta z<2\pi$	Static
9	Moving Plate w/ Turb	$\Delta z<2\pi$	Soft

3.0. Algorithms

3.1. Filtering

For each input image, the first step is to filter out the fringes and the random dot pattern so that each component can have its displacement measured individually. The filter used in this project is a hamming filter for the fringes, and a high pass filter (HPF) for the random dot pattern. The HPF utilizes the hamming filter to create the small and large circles for filtering. Both sets of data are filtered separately. The equation for the hamming filter is

$$w(n) = 0.54 - 0.46 * \cos(\frac{2\pi n}{N-1}). \tag{10}$$

When filtering out the fringes and random dots, the filter is applied to the Fourier domain of the image and channels are chosen (spots in image space) that correspond to the fringes. Mathematically this is shown as

$$f(m,n) = \frac{1}{4\pi^2} \int \int_{\omega_1, \omega_2 = -\pi}^{\pi} F(\omega_1, \omega_2) w(n) e^{j\omega_1 m} e^{j\omega_2 n}. \tag{11}$$

Figure 8 depicts the raw image to Fourier domain, and then the filtered out individual sets of data.

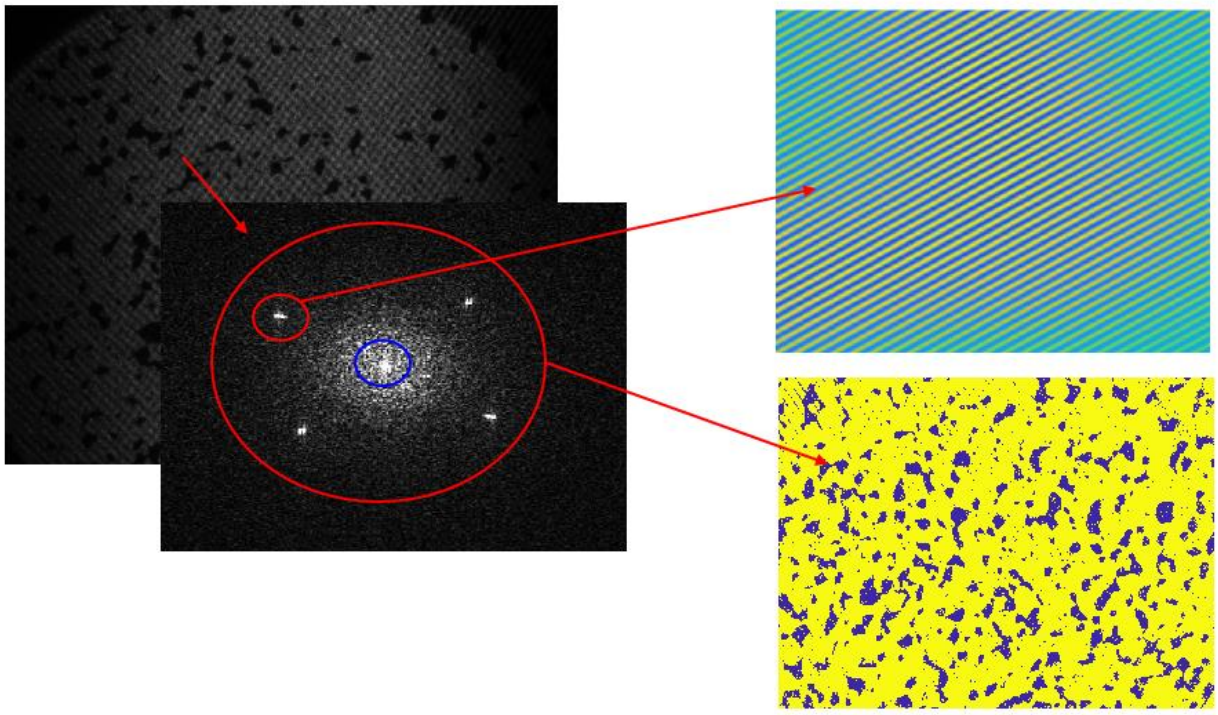

Figure 8: Top left – Raw image, Center – Fourier domain, Top right – Filtered fringe, Bottom right – Filtered random dot pattern; Circles on Fourier domain image denote hamming filter locations; blue circle denotes inner filter for high pass filter.

In the Fourier domain image shown in Figure 8, the small deltas that form a square around the center DC power are the channels for each fringe set. A delta at 90° corresponds to the fringe at 0°, 45° to -45°, and vice versa.

3.2. Fourier Phase Analysis

Phase analysis is used to start the initial displacement analysis on the fringes projected on to the object. Utilizing equation (11) the following equation is derived:

$$diff\,(m,n) = angle(\frac{fref\,(m,n)}{ftar(m,n)}). \tag{12}$$

This equation gives the difference between the reference frame and target frame, where *diff(m,n)* is in radians. This can be seen as a single pixel over time in Figure 9. Note a piezoelectric actuator is driving the object with an input sine wave, hence the shape.

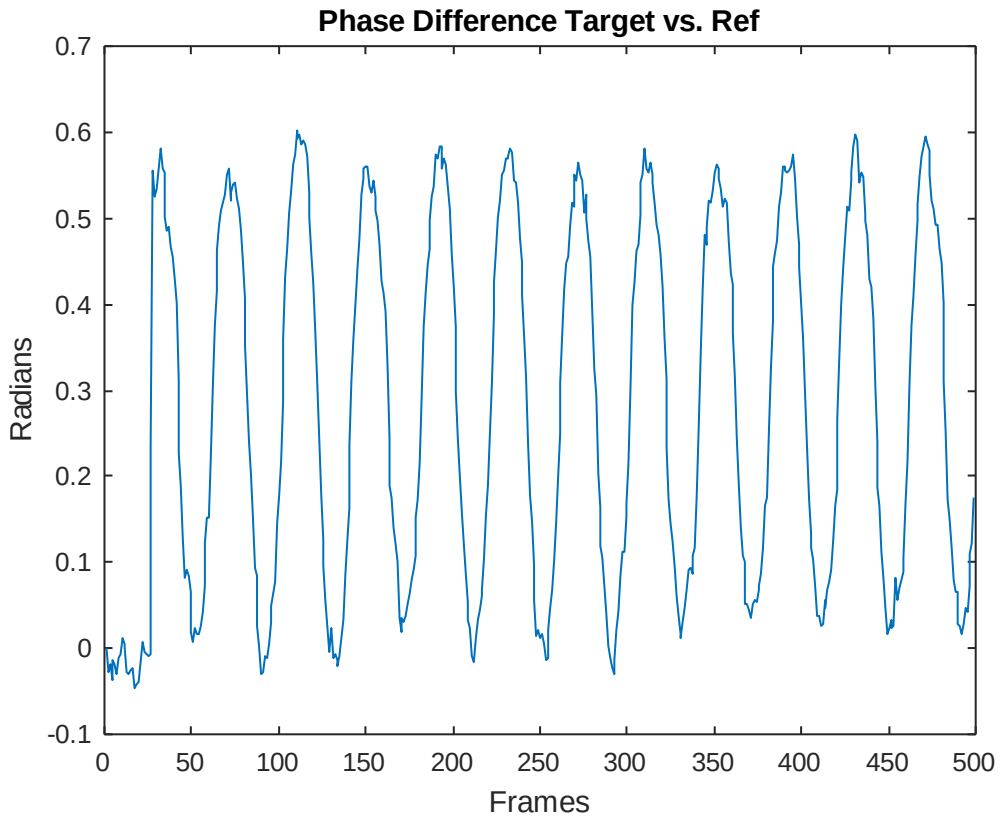

Figure 9: Phase vs. time, object being displaced a known distance using a PZT with a sine wave input

Once each variable has been established as a 3-D matrix with phase displacement data, it needs to be converted to a physical distance. This is done using the pixel per fringe value first, then applying the pixel size value:

$$f_{cam\#,fp\#} = diff(m,n) * ppf \ / 2\pi, \tag{13}$$

where ppf is pixel per fringe, and relates to a specific fringe projector. This can be different between each projector. A value in pixels is now obtained. Once multiplied by the pixel size and other geometrical features specific to the projector, a physical measurement is achieved (in microns).

3.3. Optical Flow

The optical flow algorithm used in this project comes from C. Liu [7], and is applied on the random dot pattern only. To understand more about the optical flow algorithm, refer to C.

Liu's [7] dissertation. Specifically, Appendix A in C. Liu's dissertation goes over the utilization of iterative reweighted least square (IRLS) method for optical flow in calculating *dU* and *dV* (corresponding to *x* and *y* motion) so that the gradient $\left[\frac{\partial E}{\partial dU} \quad \frac{\partial E}{\partial dV}\right] = 0$. As mentioned before, this algorithm is applied only on the random dot pattern after it has been filtered. Figure 10 shows an example from one of the tests utilizing the optical flow algorithm. In the figure, a reference image is shown to give an idea of the region of interest (ROI). This ROI is typically the center of the image filling the majority of the frame. There is an outer area where the fringe projector is not illuminating the object in the corners; this data can be ignored since optical flow requires illumination of the whole target. Figure 10 is from a test utilizing a piezoelectric actuator to move the object, so the object is moving uniformly. The *dU* flow field proves this as the values in the ROI (circled in the raw filtered image) are uniform at around -1 pixels. Since the object is moving only in the ±*Z* direction, *dV* is going to be near or at 0 (any non-zero values will come from a slight tilt in the object). To better understand why this is the case, you can refer back to the DIC overview in Chapter 1.

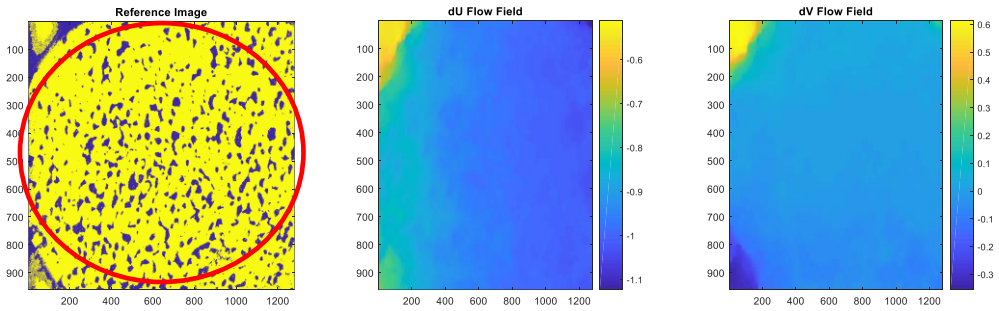

Figure 10: Images depicting a reference image for the random dot pattern, dU flow field, and dV flow field of a single frame over time.

3.4. Temporal Unwrapping

Temporal unwrapping is a very important part of this project due to the utilization of fringes in the system. If there is a large enough displacement on the target, temporal wrapping of

the fringes presents issues in solving for the fringe displacement. To solve this problem, the Goldstein branch cut method [8] of spatial unwrapping was used. To utilize this method, temporal data has to be made to look like spatial data. A pixel is taken from the image across all frames and duplicated. This is shown as

$$\sum_{n=1}^{2} X_n(n,:) = X_o(p_x, p_y,:), \tag{14}$$

where X_n is the new data to have Goldstein applied to, X_o is the original image data, and $[p_x, p_y]$ is a pixel location on the image. The colon operator indicates that pixel location across all frames. X_n becomes a 2D matrix, and Goldstein's method can now be applied to it. This needs to be done for every pixel in the image. Figure 11 shows an example of using this function in testing. In this experiment, the object was placed on a Thorlabs translation stage. For a little over 100 frames, the translation stage was moved as much as possible to cause 2π ambiguity in the fringes. This result is seen in the blue line, or the "wrapped result". After applying the Goldstein method to every pixel in the data set, we end up with a result shown as the red line. This figure only shows one pixel on one fringe projection/camera combination for reference. Notice that in this case, the fringes wrap twice throughout the frames (once in the beginning, second time towards the end). This is why it is important to have a robust unwrapping algorithm. In the case of more displacement of the object, the data will become more convoluted and will not be able to be easily unwrapped. In Section 4.1.4, the exact displacement that causes wrapping is discussed.

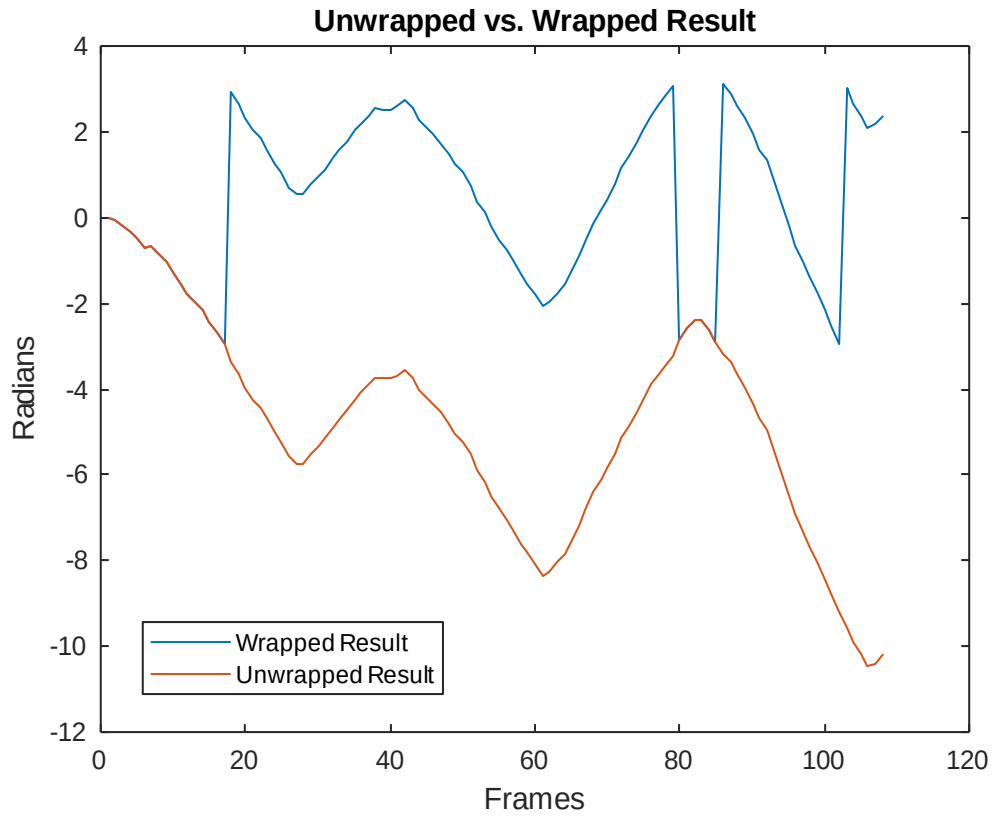

Figure 11: Wrapped vs. unwrapped result from utilizing a translation stage to force 2π ambiguity on the fringes

3.5. Matrix Algorithm

The last step for the data is to be run through the "Matrix Algorithm". A matrix was derived to both convert the units from pixels to microns, and provide a way to correct for turbulence by pulling the turbulence information out. This matrix is seen as

$$M=\begin{bmatrix} m_1\tan(\theta_1)\cos(\theta_1) & m_1 & -\dfrac{m_1\sin(\theta_1-\theta_1')}{\cos\theta_1'} & 0 \\ m_2\tan(\theta_2)\cos(\theta_2) & m_2 & 0 & -\dfrac{m_2\sin(\theta_2-\theta_2')}{\cos\theta_2'} \\ m_1\left[\tan(\theta_1)-\tan(\theta_4)\right]\cos(\theta_1) & 0 & -\dfrac{m_1\sin(\theta_1-\theta_1')}{\cos\theta_1'} & \dfrac{m_1\sin(\theta_4-\theta_4')\cos(\theta_1)}{\cos\theta_4'\cos\theta_4} \\ m_1\left[-\tan(\theta_3)+\tan(\theta_1)\right]\cos(\theta_1) & 0 & m_1\left[\dfrac{\sin(\theta_3-\theta_3')\cos(\theta_1)}{\cos\theta_3'\cos\theta_3}-\dfrac{\sin(\theta_1-\theta_1')}{\cos\theta_1'}\right] & 0 \\ m_2\left[\tan(\theta_2)-\tan(\theta_3)\right]\cos(\theta_2) & 0 & \dfrac{m_1\sin(\theta_3-\theta_3')\cos(\theta_2)}{\cos\theta_3'\cos\theta_3} & -\dfrac{m_2\sin(\theta_2-\theta_2')}{\cos\theta_2'} \\ m_2\left[-\tan(\theta_4)+\tan(\theta_2)\right]\cos(\theta_2) & 0 & 0 & m_2\left[\dfrac{\sin(\theta_4-\theta_4')\cos(\theta_2)}{\cos\theta_4'\cos\theta_4}-\dfrac{\sin(\theta_2-\theta_2')}{\cos\theta_2'}\right] \end{bmatrix}, \tag{15}$$

where θ_1 and θ_2 are both the angles of the cameras to the normal of the wind tunnel, θ_3 and θ_4 are the angles of the fringe projectors to the normal of the wind tunnel, and θ_1', θ_2', θ_3', and θ_4' are derived using the corresponding angle and estimated index of refraction of the turbulence medium. This is shown as

$$\theta_{\#}' = \arcsin\left(\frac{\sin(\theta_{\#})}{n_{\#}}\right). \tag{16}$$

$n_{\#}$ depends on which side of the system that is being considered, but should be the same for either side. The final equation for solving for the turbulence corrected answer is shown as

$$\begin{bmatrix} h'_{Rx1} \\ h'_{Rx2} \\ h'_{x21} \\ h'_{x11} \\ h'_{x12} \\ h'_{x22} \end{bmatrix} = M * \begin{bmatrix} dz \\ dx \\ t_{x1} \\ t_{x2} \end{bmatrix}, \tag{17}$$

where the left [6,1] matrix is the input data in pixels. *Rx1* and *Rx2* refer to the random dot movement (in X direction), while the last four are the individual projector and camera combinations (i.e fringe projector 1 as seen by camera 1, fringe projector 1 as seen by camera 2, and so on). The [4,1] matrix on the right is what's being solved for. Specifically, *dz* is the value for turbulence corrected motion. This gives the combined turbulence corrected result of the 6 individual components after multiplying the pseudo inverse of matrix *M* by the input [6,1] matrix. This matrix can also be used to calculate the DIC component of the system using only the first two inputs, and using only the top left [2,2] section of matrix *M*. This is important only in comparing the final results of our system to current conventional methods. The value *dz* will be used to acquire the statistical data shown in the next section.

4.0. Benchtop Testing

4.1. Results

This section utilizes Table 2 from Chapter 2, and should be referred to for a basic understanding of each test. Test 1, imaging a static object, will be omitted as it was used for noise purposes and does not pertain the system performance. Whenever the object is being displaced, it is being moved using a piezoelectric actuator driven by a signal generator. The piezoelectric actuator movement is measured using a dial indicator (referred to as "gauge" in the following plots).

4.1.1. Test 2

The first test images only the fringes. This is important to make sure the Fourier phase displacement algorithm is accurate in measuring micron displacement on its own. For this setup, a blank object is used with diffuse white paper for the fringes to be projected onto. The final result can be seen in Figure 12. This is only a plot of a single pixel location, but is similar for all pixels in the ROI. Also shown for this data set is a heat map of the mean absolute error (in microns) across the whole data set vs. the dial indicator. This is shown in Figure 13. This image is expressed as equation (18),

$$\frac{1}{N}\sum_{i=1}^{N}\left|[x,y]_i - Gauge_i\right|, \tag{18}$$

where N is the number of frames, $[x,y]$ indicates the fringe projector data (the unknown), and *Gauge* indicates the dial indicator data (the known). The typical image data set included N=200 frames. In the heat map, the ROI is circled and is similar for all proceeding tests. For this test, the average of the mean absolute error of the ROI is 1.7 μm.

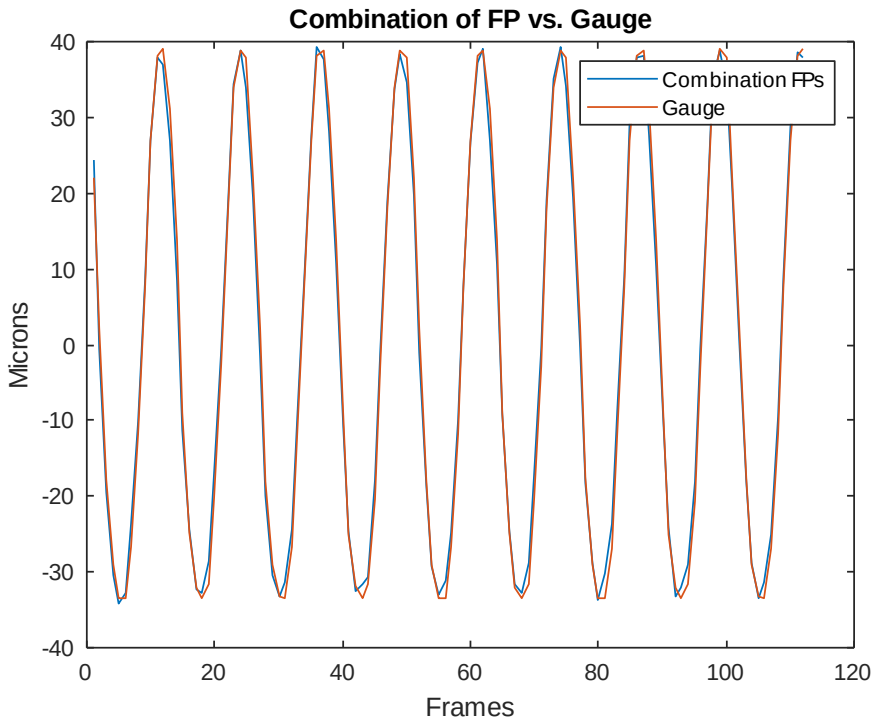

Figure 12: Fringe Projector displacement vs. actual displacement via dial indicator ("Gauge"), in microns

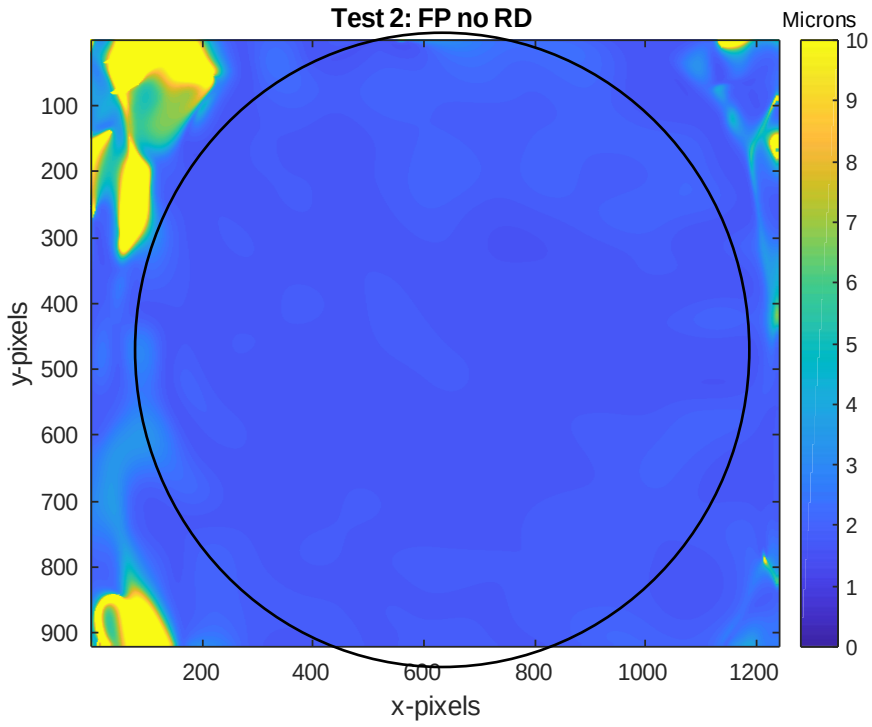

Figure 13: Mean absolute error of the fringe data vs. the dial indicator. ROI is circled

4.1.2. Test 3

The second test is the opposite of the first: image only the random dot pattern on the object, without the fringe projectors. This is done to test the accuracy of the optical flow algorithm. The setup for this test is similar to the first, except now the object has a random dot pattern painted onto it, and the optics used for creating the fringes are taken out. Figure 14 shows the single pixel over time for both the optical flow output and the dial indicator, and Figure 15 shows the mean absolute error. The average of the mean absolute error is 3.6 μm. It can be noted that ROI is not as important for this test, since the random dot pattern is not as constricted as the fringes due to the fringes only being within the 25.4 mm diameter beam. The random dots (denoted as RD in Figure 14 and onward), with enough illumination, will be processed normally.

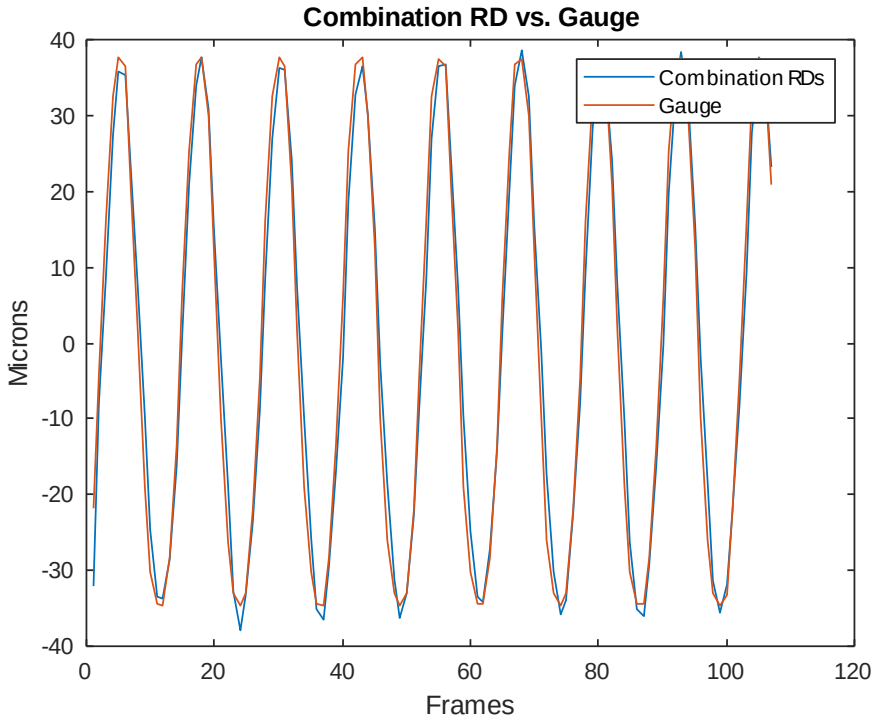

Figure 14: Optical flow output vs. dial indicator, in microns over time

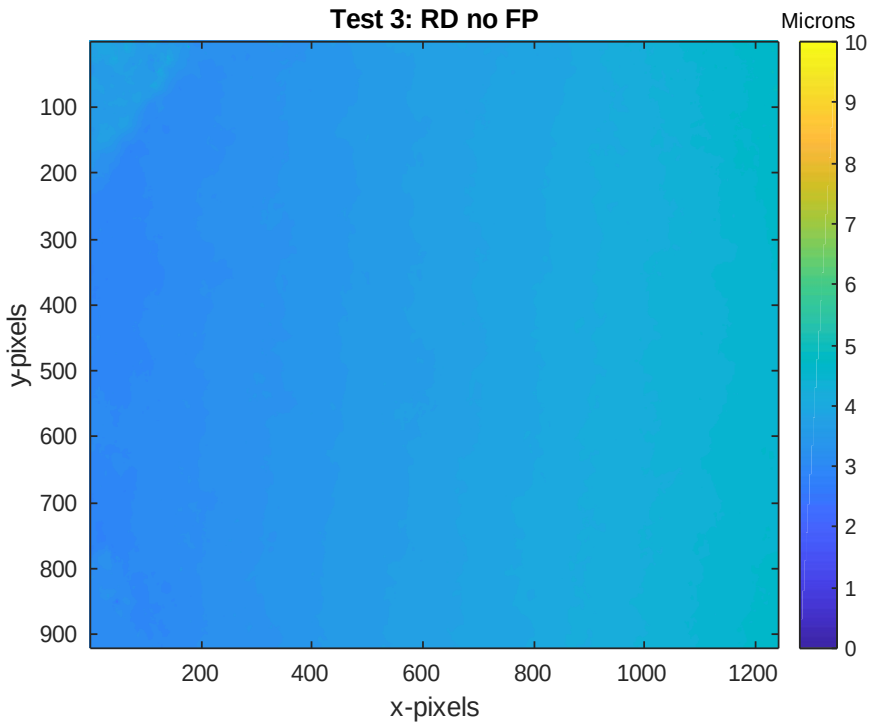

Figure 15: 2D Image of absolute mean error, note ROI not as important since the random dots are not constricted by the diameter of the projected beam

4.1.3. Test 4

The next test utilizes both the random dots and the fringes. The setup is the same, with a piezoelectric actuator and object with random dot pattern painted onto it. Fringe optics are introduced back into the system. The final algorithm combines the two together measurements together. Figure 16 shows a single pixel over time and Figure 17 shows the mean absolute error, with the average error of the ROI being 2.3 μm.

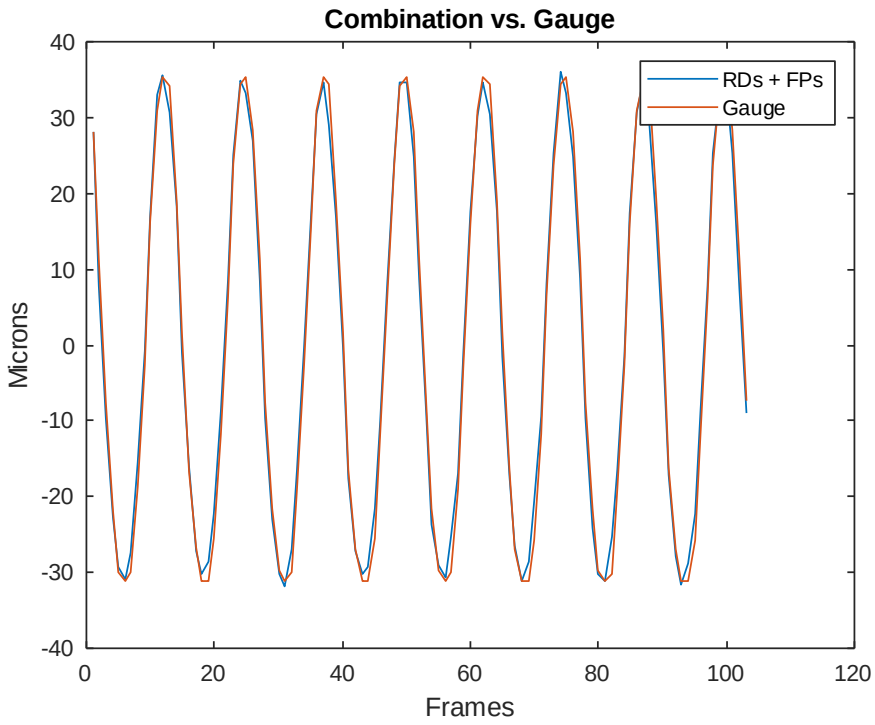

Figure 16: Combination of random dots and fringes output vs. dial indicator, in microns over time

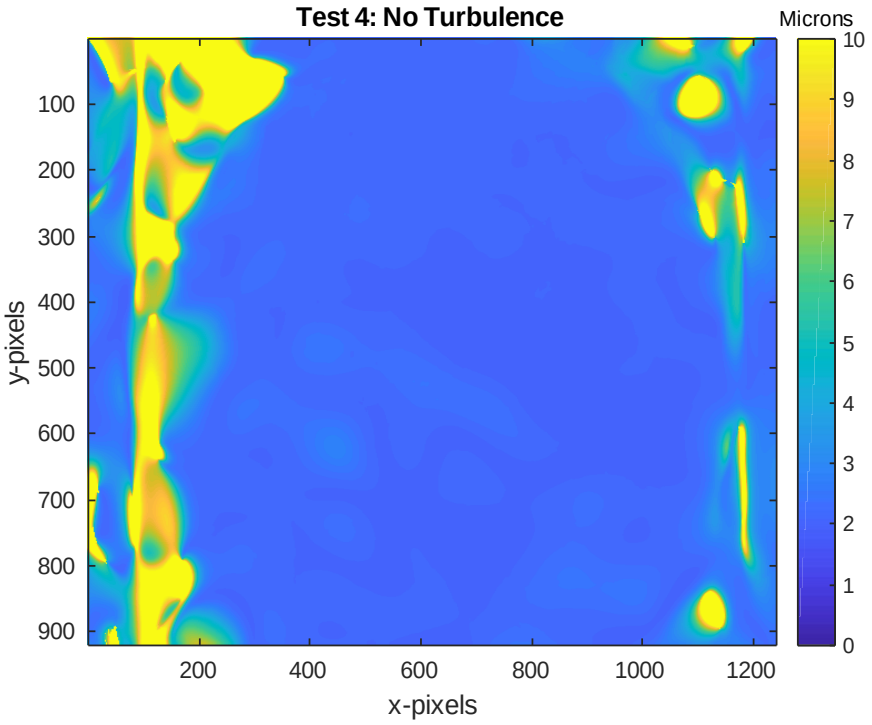

Figure 17: Mean absolute error

4.1.4. Test 5

The last test before introducing simulated turbulence into the system is testing the fringes and random dot algorithms with motion that causes 2π ambiguity in the fringes. This will also be closer to displacement seen in a wind tunnel, as over 100 μm in displacement will be seen. For this test, a Thorlabs translation stage is used to create large displacement. When the system is turned on, the translation stage is moved by hand with the dial indicator measuring the displacement of the target. In the plot showing a single pixel location, three lines are shown: line for dial indicator ("gauge") measurement, line for wrapped data before unwrapping, and line for unwrapped data using Goldstein method. The wrapped data is used for comparison to show where the fringes wrap in microns. Two points are displayed to indicate that the fringes wrap at a total displacement of 168.9 μm. The average of the mean absolute error heat map within the ROI is 11.9 μm. It is noticed here that as the translation of the object becomes larger and more randomized, average error increases. This is likely due to as displacement is increased, more room for error is introduced.

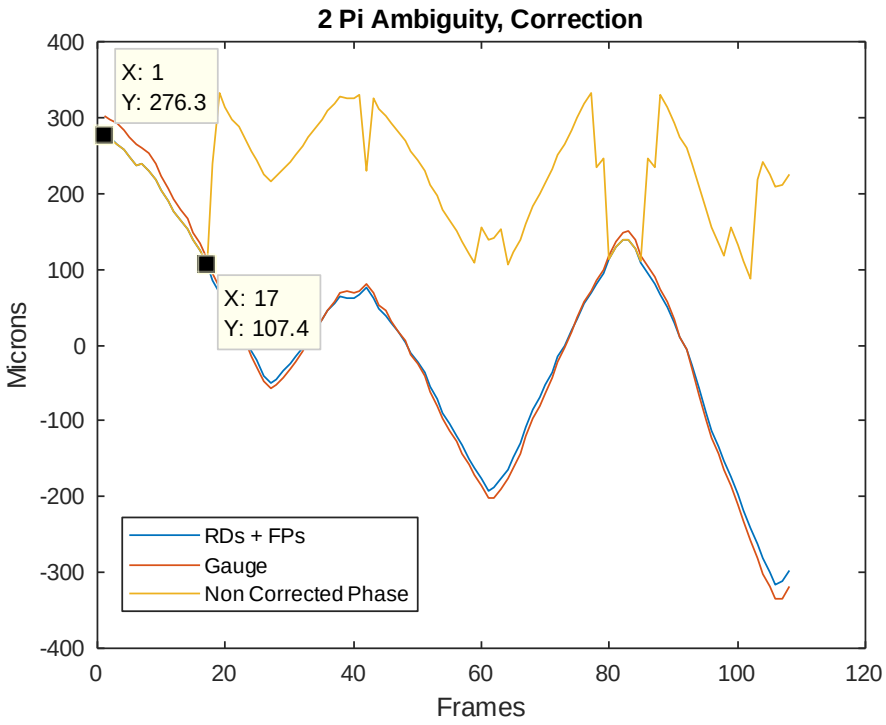

Figure 18: Plot showing gauge data, wrapped data, and unwrapped data. Two points shown for where wrapping occurs, in microns

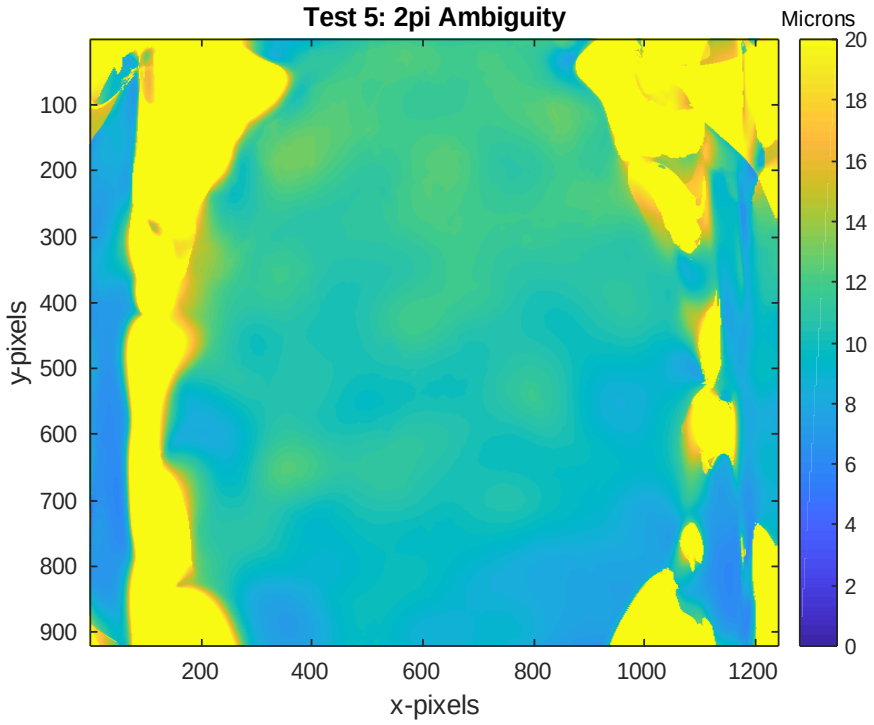

Figure 19: Mean absolute error

The next milestone in testing the system is adding simulated turbulence. There are two types of simulated turbulence used, static turbulence and soft turbulence. More on how these tests are conducted is discussed in Section 2.3: Experimental Setup and Testing. For these tests, two data sets are recorded. The first is used to acquire a calibrated Matrix *M* (calibrated for the turbulence seen in data set 1). This matrix *M* is then applied to data set two, which should see different randomized turbulence. This is done to test the accuracy of calibrating the matrix before applying it to a wind tunnel run with unknown turbulence affects. There are 4 tests related to the use of this turbulence. These tests are described in the following Sections 4.1.5 through 4.1.8.

4.1.5. Test 6

The first two tests utilize each form of simulated turbulence with no target movement. In this case the measured displacement will come from turbulence, as the actual fringe displacement and random dot displacement on the object should be 0 μm. Test 6 uses the cover glass to simulate static turbulence with the non-moving target. Figure 20 shows the mean absolute error, with the average of this error within the ROI at 11.1 μm. From Figure 20, the error is not as uniform as would be expected when utilizing a piece of glass with uniform tilt and flatness. This is likely due to the target not being completely orthogonal to normal. It is also likely the flatness of the piece of glass is not measured to a low tolerance, and will have deviations in the micron range. The error is also going to be slightly higher than that of the use of soft turbulence. This is because the glass presents a worst case scenario, as the index of glass is going to be exponentially higher than that of perturbed air, even at the low thickness that is presented. With this higher turbulence case, there are going to be errors in the matrix correction at some pixel locations. This is shown as pixelated areas within the ROI.

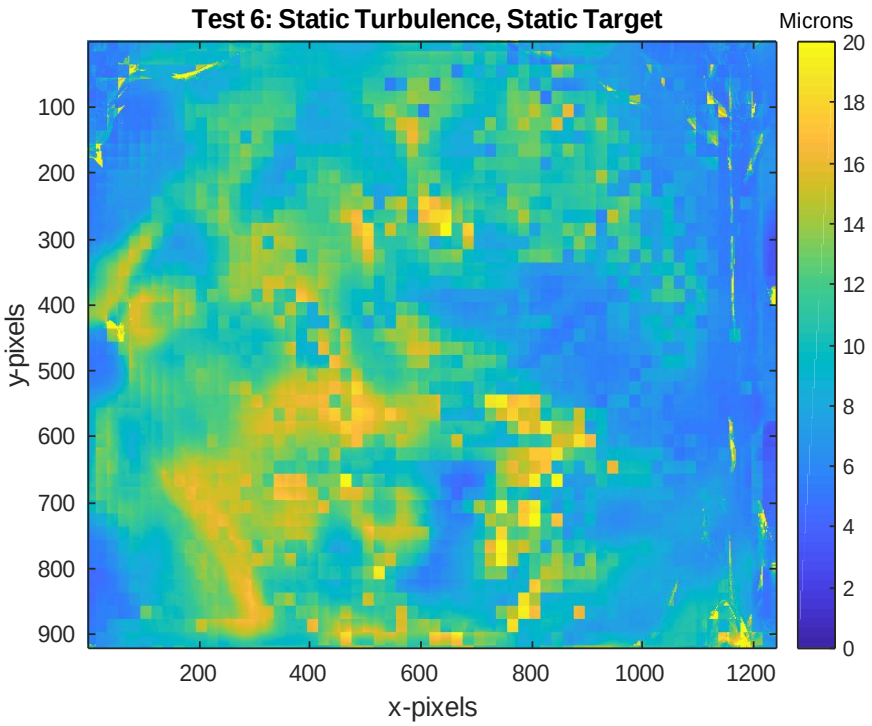

Figure 20: Mean absolute error

4.1.6. Test 7

Test 7 repeats test 6 work, using soft turbulence in the form of a nichrome wire. Mean absolute error is shown below in Figure 21, with an average of 6.9 μm. Error on the right side of the heat map is much higher than the rest. This is due to two reasons: that side of the beam likely took on more turbulence than the rest of the system (since it is randomized, this could happen in many cases to different parts of the ROI), and part of that side is not within the ROI indicated in Figure 13.

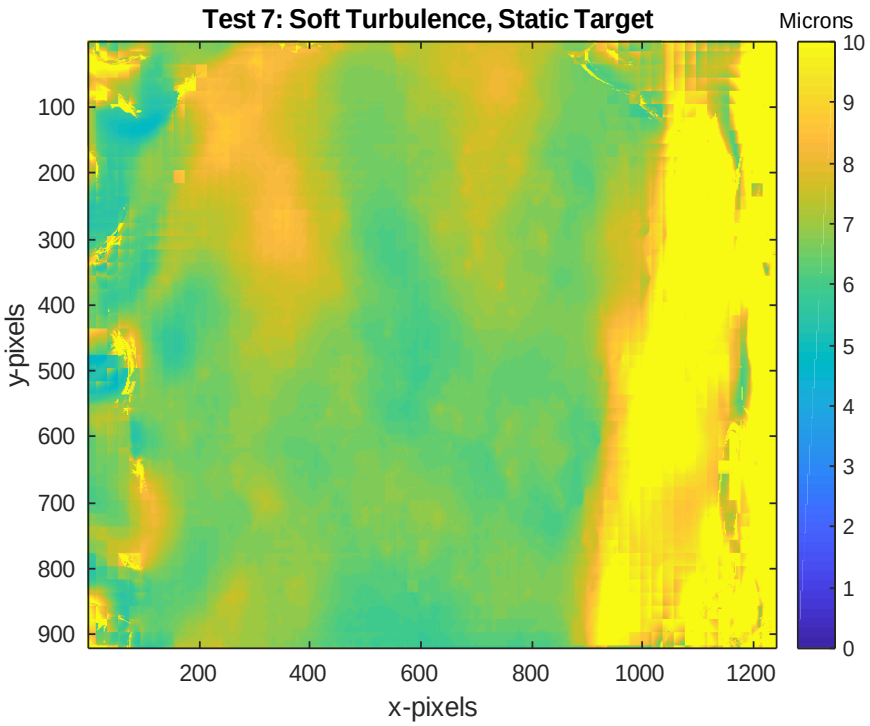

Figure 21: Mean absolute error

4.1.7. Test 8

Tests 8 and 9 repeat tests 6 and 7, however now using a moving homogenous target. Test 8 uses the simulated static turbulence. Mean absolute error is shown below in Figure 22, with an average error of 15.1 μm. An increase in average error within the ROI of both these tests is expected now that there are conflicting displacement measurements (turbulence seen displacement and true target displacement).

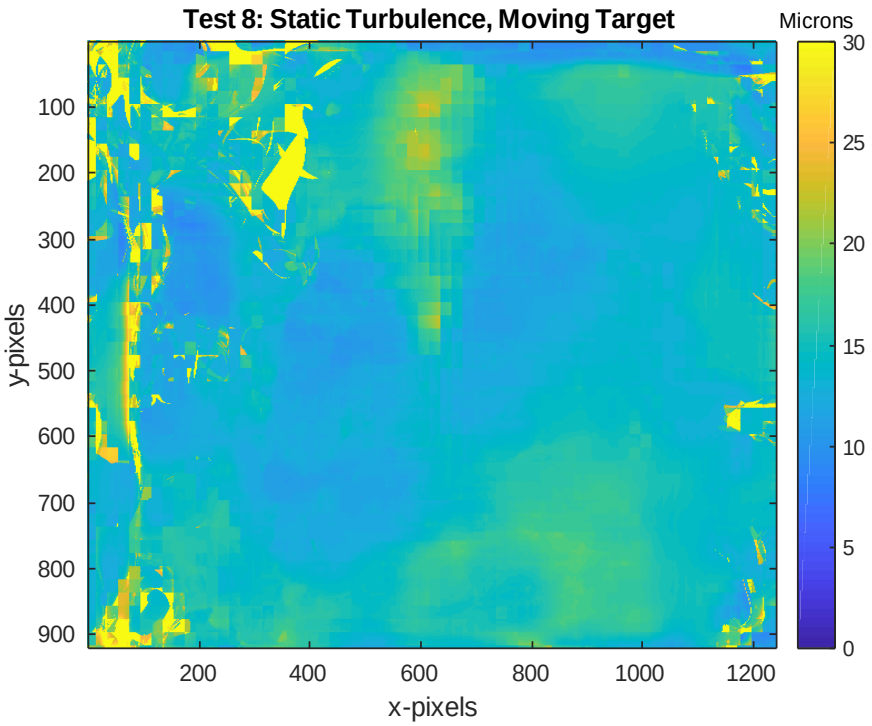

Figure 22: Mean absolute error

4.1.8. Test 9

Test 9 consists of multiple tests. The reasoning for this is to acquire as much simulated soft turbulence as possible. The first test involves the normal straight nichrome wire. The second test utilizes the same wire, but folded in a zig-zag pattern to create more volumetric turbulence. The third test utilizes a heat gun to simulate an accelerated turbulence environment (i.e turbulence moving from left to right, at a higher velocity). Results are depicted in Figures 23 (a), (b), and (c) respectively. The average of the ROI of these heat maps is 7.7 μm (a), 10.0 μm (b), and 6.9 μm (c).

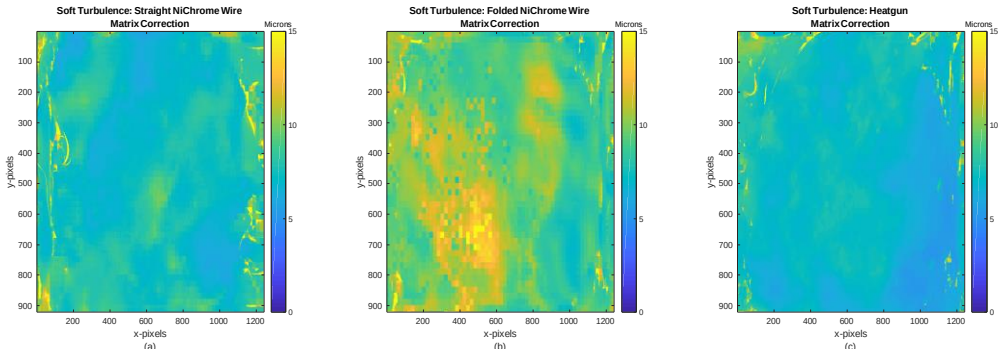

Figure 23: Mean Absolute Error of each individual soft turbulence case with moving homogenous target

4.2. System Performance vs. DIC

Now that the performance of each individual system is characterized and has been put through tests to acquire its accuracy in the presence of simulated turbulence, the next step is to compare its performance to a normal DIC system. Figure 24 shows the matrix calibrated results (Figure 24 (a), (b), and (c)) versus their corresponding DIC results (Figure 24 (d), (e), and (f)). These results are from conditions using test 9. The result for DIC shows on average a mean absolute error of 10.7 μm (d), 13.9 μm (e), and 10.3 μm (f). The current performance of the new system shows on average a mean absolute error of 7.7 μm (a), 10.0 μm (b), and 6.9 μm (c). This shows an improvement in error from DIC. However, the ROI leaves something to be desired, sitting at a little less than 25.4 mm in diameter and missing a lot of the edge cases of the image. The ROI of the DIC system is larger, getting a more uniform result around the edges as it relates to our depicted ROI from Figure 13. Any non-uniformity of the DIC system (around the edges where the beam illuminates the object) would come from the use of a collimated beam to illuminate the target, and can be fixed using better lighting.

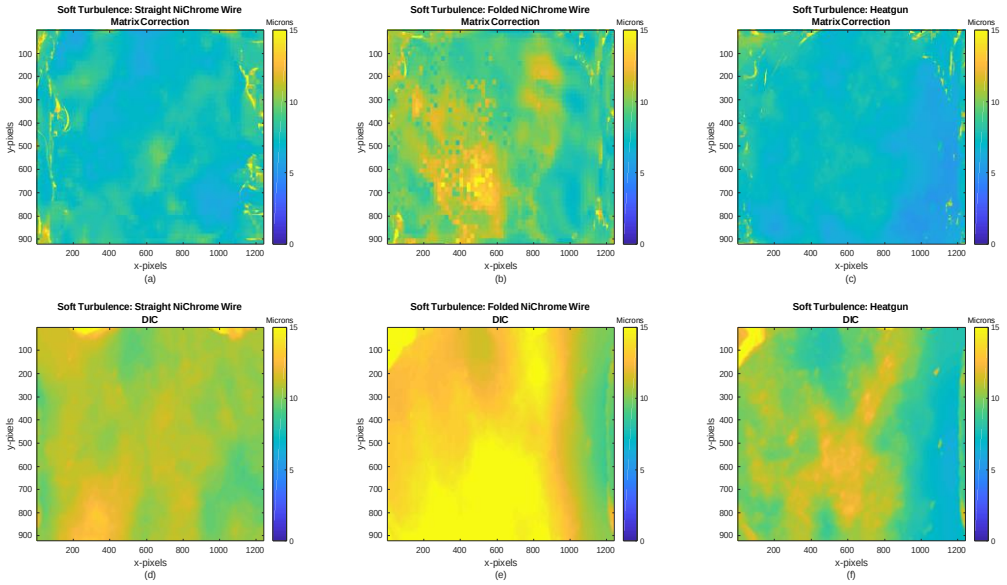

Figure 24: Each individual test 8 soft turbulence case with Matrix correction vs. DIC output

5.0. Conclusion and Future Work

This thesis describes a novel method of measuring the displacement on objects in a hyper velocity environment (such as a hypersonic wind tunnel). In the case of the current work, simulated turbulence is used in place of a hypersonic wind tunnel to test the system and compare its performance to Digital Image Correlation (DIC), the current method used in measuring displacement in such environments. Also in this thesis, only 25.4 mm optics are used to make sure the system works before scaling up to the full 150 mm system. Results from Section 4.2 indicate that this new system improves the mean absolute error of DIC methods from 10.7 μm to 7.7 μm on average (for the first soft turbulence case with a moving target). The results from Chapter 4 indicate great performance in comparison to the project goals, achieving a measurement error much less than the ±30 μm desired accuracy.

5.1. Future and Ongoing Work

Future work to be completed on testing the system is switching out a homogenous target to a deformable one. This would allow the system to work with a target that would be more comparable to an object being deformed inside of a hypervelocity environment. Once this is completed, taking the 25.4 mm system to a hypersonic wind tunnel would allow for final tests before scaling up towards the 150 mm system.

Ongoing work involving the algorithms includes attempting to utilize a neural network to correct for turbulence aberrations in the scene instead of using the derived matrix from Section 3.5. At present, the matrix only accounts for tilt and not any higher order modes created by the hypervelocity environment. A neural network could provide correction to these higher orders. The network takes in the two random dot displacements in pixels, the four fringe/camera pair displacements in pixels, and the dial indicator data as data for training from one test. That is then

applied to a separate test to assess accuracy. Preliminary results from this testing shows slight improvement over the matrix with an average mean absolute error of 6 μm (a) compared to 7.7 μm (b) and 10.7 μm (c).

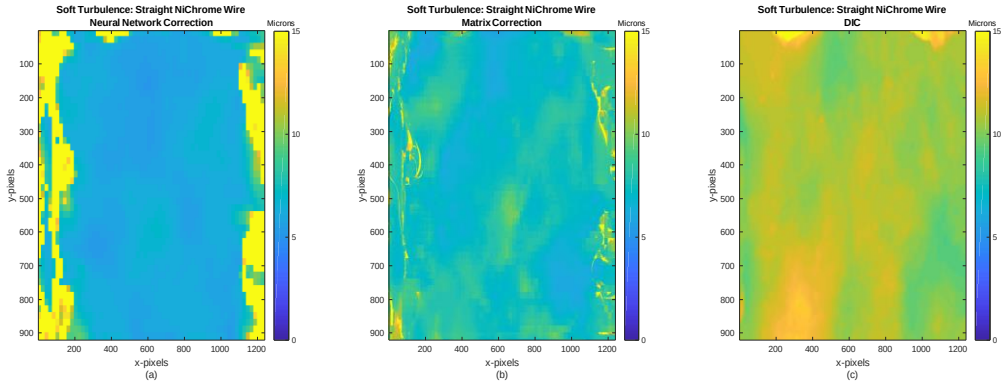

Figure 25: Comparison of Neural Network (a) correction to Matrix (b) correction and DIC (c), mean absolute error values

REFERENCES

[1] Pan, Bing, et al. "Two-dimensional digital image correlation for in-plane displacement and strain measurement: a review." Measurement science and technology 20.6 (2009): 062001.

[2] Pan, B., et al. "Accurate measurement of satellite antenna surface using 3D digital image correlation technique." Strain 45.2 (2009): 194-200.

[3] Rastogi, Pramod K., ed. Photomechanics. Vol. 77. Springer Science & Business Media, 2003.

[4] Creath, Katherine. "Phase-measurement interferometry techniques." Progress in optics 26.26 (1988): 349-393.

[5] Gens, Rudiger, and JOHN L. VAN GENDEREN. "Review Article SAR interferometry—issues, techniques, applications." International Journal of Remote Sensing 17.10 (1996): 1803-1835.

[6] Vanderwerf, Dennis Frank. Applied prismatic and reflective optics. SPIE Press, 2010.

[7] Liu, Ce. Beyond pixels: exploring new representations and applications for motion analysis. Diss. Massachusetts Institute of Technology, 2009.

[8] Goldstein, Richard M., Howard A. Zebker, and Charles L. Werner. "Satellite radar interferometry: Two-dimensional phase unwrapping." Radio science 23.4 (1988): 713-720.